Contemporaneous formation of chondrules and refractory inclusions in the early Solar System

Shoichi Itoh & Hisayoshi Yurimoto

Department of Earth and Planetary Sciences, Tokyo Institute of Technology, Meguro, Tokyo 152-8551, Japan

Chondrules and calcium-aluminium-rich inclusions (CAIs) are preserved materials from the early history of the Solar System, where they resulted from thermal processing of pre-existing solids during various flash heating episodes which lasted for several million years[1]. CAIs are believed to have formed about two million years before the chondrules[2–5]. Here we report the discovery of a chondrule fragment embedded in a CAI. The chondrule's composition is poor in ^{16}O, while the CAI has a ^{16}O-poor melilite (Ca, Mg, Al-Silicate) core surrounded by a ^{16}O-rich igneous mantle. These observations, when combined with the previously reported CAI-bearing chondrules[6–9], strongly suggest that the formation of chondrules and CAIs overlapped in time and space, and that there were large fluctuations in the oxygen isotopic compositions in the solar nebula probably synchronizing astrophysical pulses.

The chondrule-bearing CAI, which we have designated A5, was found in the Y-81020 CO3.0 chondrite (Fig. 1). The CAI is about 100 μm across, and consists of a large central polycrystalline melilite (10–13% åkermanite;$Åk_{10–13}$) clast and a three-pyroxene assemblage enclosed by a porous glassy mesostasis (Supplementary Fig. 1). The mesostasis consists of Al-rich clinopyroxene filaments embedded in Al-rich glass. These textures indicate that the mesostasis was quenched from a liquid. The pyroxene assemblage includes troilite and metal, as well as enstatite, augite and pigeonite. This assemblage has not previously been observed in CAIs[10], and the chemical compositions of the pyroxene phases (Table 1) are also not known from CAIs. However, such an assemblage is typical of chondrules[11]. Thus, it is evident that the pyroxene assemblage is a fragment of a chondrule, which has mineralogical and textural properties similar to the most frequently observed type-I (that is, low FeO) porphyritic chondrules in the CO chondrites.

The oxygen isotope data are bimodally distributed on the carbonaceous chondrite anhydrous minerals (CCAM) line (Fig. 2). All the ^{16}O-rich values are from the mesostasis. The O isotope values in both the melilite clast and the pyroxene assemblage are depleted in ^{16}O. We emphasize that the O isotopic composition of the pyroxenes falls within the range observed in low FeO (type-I) CO chondrules[12,13]. The non-mass-dependent O-isotope distribution indicates that the large melilite crystals in the CAI, and the chondrule fragment (that is, enstatite, pigeonite and augite), did not crystallize from or equilibrate with the surrounding mesostasis liquid.

This non-equilibrium state is also supported by the elemental composition of the mesostasis. The mesostasis composition (Table 1 and Supplementary Table 1) corresponds to the type-C CAI field of Stolper's diagram[10,14]. This composition shows that spinel and then

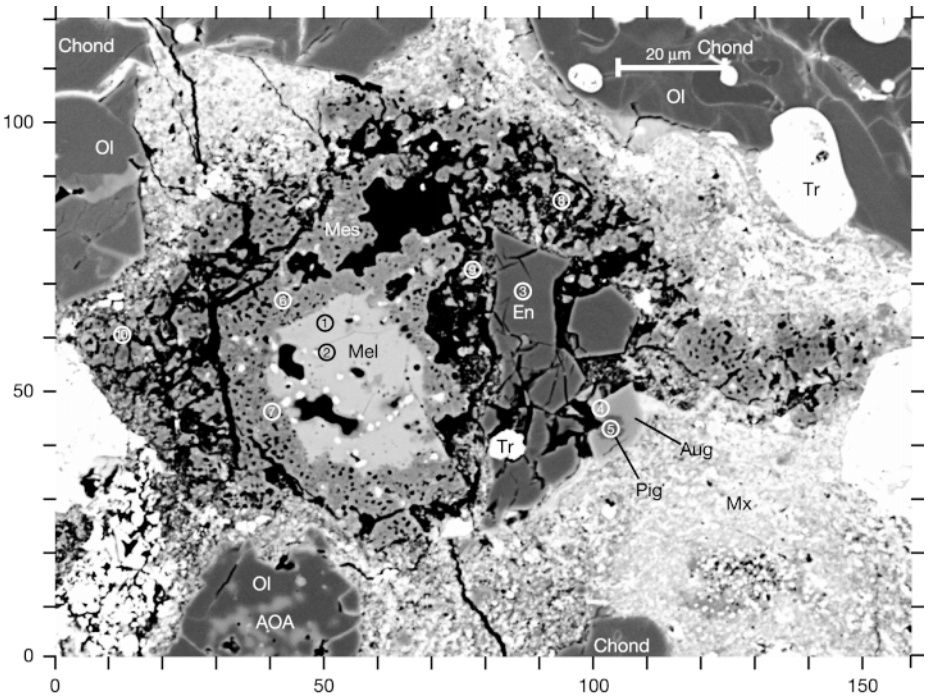

Figure 1 Back-scattered electron image of the chondrule-bearing CAI. The object, named A5, was found in a thin section (no. 56-4 from the National Institute of Polar Research, Tokyo) of the Y81020 CO3.0 chondrite. Horizontal and vertical scales are in μm. Scale bar also at top right. Locations of SIMS analyses are shown by numbers corresponding to those in Table 1. The circle size round each number shows the approximate analytical area of O isotopic composition by SIMS. The CAI consists of a large central polycrystalline melilite ($Åk_{10–13}$, Mel) clast in which individual melilite crystals are about 20 μm across. Fine perovskite grains (white spots) are scattered in and around the melilite. The melilite clast is enclosed by a porous mesostasis (Mes) composed of a fine-grained mix of Al-rich clinopyroxene (lighter area; MgO, 13.3 wt%; Al_2O_3, 18.1; SiO_2, 37.5; CaO, 24.2; TiO_2, 6.3; other elements <0.1) and Al-rich glass (darker area; MgO, 7.0–10.6 wt%; Al_2O_3, 41.2–43.9; SiO_2, 24.6–33.3; CaO, 11.7–16.7; TiO_2, 0.6–1.9; Cr_2O_3, 0.3–1.0; FeO, 0.3–1.2; other elements <0.1). Also enclosed by the porous mesostasis is a pyroxene assemblage dominated by enstatite (En) with minor pigeonite (Pig) and augite (Aug). The augite is an overgrowth on the pigeonite. Troilite (Tr) is minor phase associated with the pyroxene assemblage. Troilite and Fe-Ni metal (white spots) are scattered in the mesostasis near the pyroxene assemblage. The right lower side of the CAI is broken surface where the pyroxene assemblage directly borders the matrix (Mx). Other abbreviations: Ol, olivine; Chond, chondrule; AOA, amoeboid olivine aggregate.

anorthite would be the first phases to crystallize, but these are not present in A5. The absence of spinel in the mesostasis implies that the mesostasis quenched at >1,550 °C (ref. 14). It is believed that the type-C CAIs result from melting precursor refractory condensates from the nebular gas[10], giving rise to the ^{16}O-rich composition of the mesostasis. Thus the ^{16}O-rich mesostasis directly shows that the melting process related to CAI formation.

If CAIs formed before chondrules, then the mesostasis in A5 melted again during the chondrule-forming event. If this sequence of events occurred, CAIs and chondrules should have coexisted in the chondrule-forming region and should have melted by the second melting event of the mesostasis. However, igneous CAIs are rare in CO chondrites[15]. Most of CAIs in CO chondrites were formed by condensation of solids[10].

The quench texture of the mesostasis suggests that the cooling rate of the CAI was faster than those of typical coarse-grained CAIs[16]. Small O isotopic zoning in the rim of the melilite clast (Fig. 2, Supplementary Figs 2 and 3, Supplementary Table 2) indicates that the melting event partly exchanged O isotopic composition of the melilite with the ^{16}O-rich mesostasis melt by O self-diffusion. The cooling rate can be evaluated by the O isotopic zoning (Supplementary Fig. 3) and the O self-diffusion coefficient of $\mathring{A}k_{12}$ (ref. 17). According to the compensation timescale[18] and assuming a non-moving surface, the cooling rate, s (in K s^{-1}), is given by: $\log s = [(-1.8\times10^4)/T_0] + 8.8$ along the a axis of melilite, and $\log s = [(-1.6\times10^4)/T_0] + 6.8$ along the c axis, where T_0 is absolute temperature at the start of diffusion. Based on these parameters, the cooling rate of the chondrule-bearing CAI was several hundreds to several tens of degrees per hour if $T_0 = 1{,}823$ K (estimated liquidus temperature of the mesostasis), indicating a faster cooling rate than that of most CAIs[16].

Because the melilite clast is completely surrounded by ^{16}O-rich mesostasis, the ^{16}O-poor values of the melilite are plausibly the original O-isotopic composition of the melilite clast. The preservation of the original O-isotopic compositions is consistent with the observation that the CO3.0 chondrites are remarkably pristine, having experienced very little thermal metamorphism or aqueous alteration[15,19,20]. In particular, no evidence of O isotopic disturbance has been observed in fine-grained melilite from CO3.0 chondrites[21]. The large grain size of melilite in the clast (Fig. 1) and preservation of ^{16}O-rich glass in the mesostasis next to the ^{16}O-poor melilite clast (Fig. 1, Table 1) also support the suggestion that the O isotopic composition of the melilite clast has not been disturbed after mesostasis formation.

On the basis of these petrological and isotopic results, we conclude that the A5 CAI contains a fragment of a chondrule. This chondrule fragment survived the last melting event in the formation of the CAI, probably because of the short duration of heating and cooling. The chondrule fragment must have formed before the last melting episode of the CAI, which indicates that the formation of the chondrule and the formation of the CAI overlapped, at least partly, both in time and in space. Another important finding in the CAI is that a ^{16}O-rich liquid encloses a relict CAI melilite fragment with a more ^{16}O-poor composition. This indicates that O-isotopic variation in CAIs occurred in the solar nebula, and did not monotonically change from ^{16}O-rich to ^{16}O-poor. Therefore, the O-isotopic composition of solids in the solar nebula did not uniformly evolve from ^{16}O-rich to ^{16}O-poor.

Oxygen is the most abundant element in solid phases and is third in abundance, after H and He, in the solar nebula gas. Thus O isotopes are appropriate tracers of material evolution and global changes in the solar nebula. The O isotopic variation of the chondrule-bearing CAI may be understandable within the framework of the X-wind model[22]: this model offers a mechanism for the bipolar jet and X-ray flare of proto-stars[22], for contemporaneous formation of CAIs and chondrules around the inner edge of the

Table 1 **Oxygen isotopic compositions (‰) and chemical compositions in A5 inclusion**

Phase	Melilite		Enstatite	Augite	Pigeonite	Mesostasis						
No. in Fig. 1	1	2	3	4	5	6	6	6	7	8	9	10
Beam overlap	None	None	None	None	Augite 10%	None	None	None	Melilite 5%	None	–	None
Oxygen isotopic compositions (‰)												
$\delta^{17}O_{SMOW}$	−7.5	2.0	−7.4	4.1	−11.2	−34.3	−22.8	−37.8	−25.0	−30.4	–	−35.2
σ_{mean}	2.9	2.5	2.4	2.6	2.3	2.3	3.1	2.1	2.3	2.6	–	2.6
$\delta^{18}O_{SMOW}$	0.2	7.7	−1.4	8.2	−2.9	−31.8	−20.2	−36.8	−21.7	−25.1	–	−33.3
σ_{mean}	1.2	1.4	1.8	1.4	1.4	2.1	1.2	1.3	2.1	2.4	–	1.6
Chemical compositions (wt %)												
MgO	2.0	1.7	38.6	21.0	34.4			7.1	7.0	10.0	15.3	12.8
Al_2O_3	32.8	34.8	1.2	2.4	1.5			31.9	32.4	26.7	24.5	32.0
SiO_2	25.2	22.8	59.5	55.1	55.4			23.0	28.0	22.9	34.8	24.4
K_2O	ND	ND	ND	ND	ND			ND	ND	ND	ND	0.2
CaO	42.7	40.1	0.6	20.5	3.3			14.4	17.8	8.7	9.6	9.7
TiO_2	ND	ND	ND	ND	0.1			0.9	1.8	1.8	0.8	1.8
Cr_2O_3	ND	ND	ND	0.6	0.3			0.3	ND	0.7	0.4	ND
FeO*	ND	ND	0.6	0.8	2.1			1.0	2.2	8.7	1.4	13.4
Ni*	ND	ND	ND	ND	ND			ND	ND	0.9	ND	0.9
S	ND	ND	ND	ND	ND			ND	ND	0.4	ND	0.2
Total	102.7	99.4	100.5	100.4	97.1			78.7	89.2	79.4	86.8	94.2
Chemical formulae												
O	7	7	3	6	3							
Mg	0.13	0.11	0.96	1.11	0.90	Stolper's mode (wt%)						
Al	1.72	1.88	0.02	0.10	0.03	Forsterite		6	8	15	28	15
Si	1.12	1.05	0.99	1.96	0.97	Anorthite		54	56	63	72	55
Ca	2.04	1.97	0.01	0.78	0.06	Gehlenite		20	23	0	−8	3
Ti	ND	ND	ND	ND	0.00	Spinel		21	12	22	8	27
Cr	ND	ND	ND	0.02	0.00							
Fe	ND	ND	0.01	0.02	0.03							
Iotas cation	5.02	5.01	1.99	3.99	2.01							

Oxygen isotopic compositions and chemical compositions of each major phase were measured by secondary ion mass spectrometry (using TiTech Cameca ims 1270) and X-ray microanalysis (using JEOL JSM-5310LV scanning electron microscope + Oxford LINK-ISIS energy dispersive X-ray spectrometer), respectively. The analytical methods are described elsewhere[30]. Beam overlap, area fractions of inadequate phases in the sputtering crater. σ_{mean}, standard deviation of the mean determined by statistical variation of secondary ion intensities corresponding to precisions for a series of measurements. The accuracy (2σ) of the δ-values is estimated to be ± 7.1‰ for $\delta^{17}O$ and ± 5.7‰ for $\delta^{18}O$. Three independent analyses were made at position 6. Concentrations of phenocrysts and mesostasis were determined at or near the sputtering craters by spot electron beam (~1 μm) and by rastering beam (~7 × 7 μm), respectively. Low totals for the mesostasis are due to the porous structure. FeO*, all Fe calculated as FeO. Ni*, all Ni calculated as Ni. ND, not detected (<0.1 wt%). Stolper's mode, according to ref. 14.

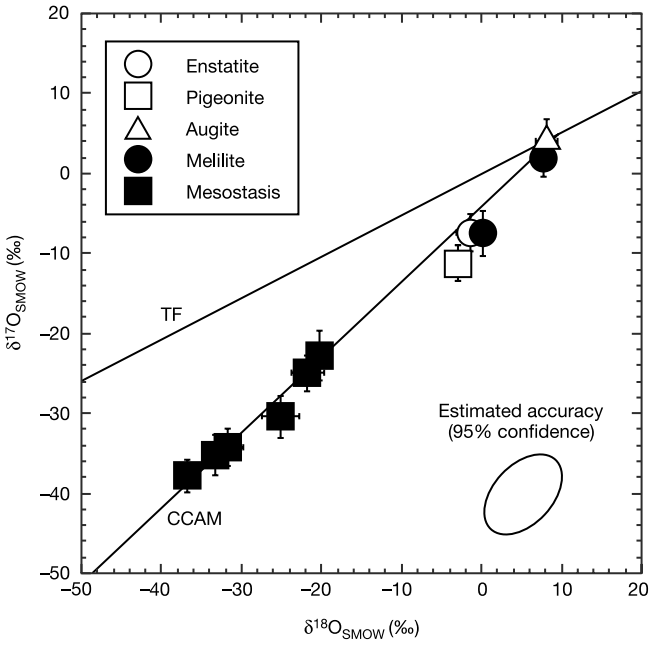

Figure 2 Oxygen-isotopic composition of minerals in the chondrule-bearing CAI. Error bars of individual analyses denote standard deviations corresponding to precisions for a series of measurements (Table 1). Accuracy (95% confidence), estimated from repeated measurements of standard materials, is denoted at lower right. Abbreviations: TF, terrestrial fractionation line; CCAM, carbonaceous chondrite anhydrous mineral mixing line[26]. All phenocrysts depleted in ^{16}O are embedded in Ca-Al-rich glassy mesostasis that is ^{16}O-rich. Because O isotopic compositions in the melilite clast were measured in sequence during the same analytical session, the difference between the two δ-values in the melilite is much larger than the analytical precisions (also see Supplementary Fig. 2 and Supplementary Table 2). The O isotopic zoning of the melilite clast (more ^{16}O-rich towards rim) is probably due to O isotopic diffusion during cooling of the last melting event. The ^{16}O-rich mesostasis seems to be slightly inhomogeneous in its oxygen isotopes. This can be explained by aqueous alteration in the parent body because of rapid O diffusivity in glass. Despite the alteration, the secondary O isotopic modifications are partial because the Al-rich glass mostly occupies the sputtered areas of SIMS analysis.

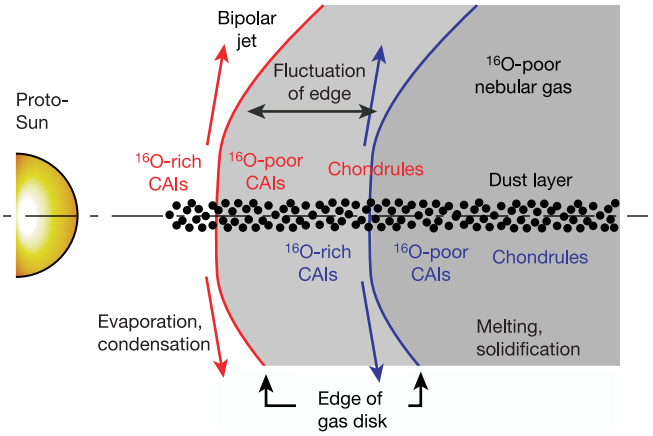

Figure 3 Schematic view of CAI and chondrule formation. The solar nebula originally consisted of ^{16}O-rich dusts and ^{16}O-poor gas[26]. CAIs having a ^{16}O-rich signature formed at the inside of the inner edge of the gas disk. CAIs with ^{16}O-poor signature and chondrules formed in the gas disk. Expected radial excursions of the X-point[22] are shown as red and blue colours. CAIs having both ^{16}O-rich and ^{16}O-poor signatures formed at the fluctuation zone of the inner edge. O isotopic exchange of CAI minerals occurred when the ^{16}O-rich CAI was embedded in the gas disk.

solar nebula (the X-point)[22], for compound objects consisting of a CAI core and a chondrule mantle[23,24], and for potential cyclic variation of the O-isotopic composition in the formed solids[25].

Chondrules and CAIs were possibly formed by X-ray-flare heating, arising as a result of the time-dependent interaction of a protoplanetary disk with the protosolar magnetosphere[22]. Figure 3 is a schematic view of the CAI- and chondrule-forming region around the inner edge of the protosolar disk. In the steady state, ^{16}O-rich solids[26] form ^{16}O-rich CAIs at the proto-Sun side of the X-point where the ^{16}O-poor gas[26] is ionized and removed by the strong electromagnetic forces[22]. This region therefore results in a very high dust/gas ratio[27]. Evaporation, condensation and melting of dusts by the flare heating form ^{16}O-rich CAIs. Chondrules form outward of the X-point, where the precursor solids are immersed in ^{16}O-poor gas. Chondrules therefore tend to have ^{16}O-depleted O-isotopic compositions. ^{16}O-poor CAIs[28] would form in the region between the forming regions of ^{16}O-rich CAIs and of ^{16}O-poor chondrules. However, the O isotopic variation observed in A5 indicates that ^{16}O-rich and ^{16}O-poor materials were gathered into one object, suggesting O isotope oscillation in the nebular regions where CAIs and chondrules formed.

The radial excursions of the X-point occurred repeatedly on relatively short timescales, with cycles ranging from days to thousands of years[22]. Synchronously the dust-to-gas ratio in the fluctuation zone changed, owing to the radial fluctuation of the inner edge of the gas disk. On the other hand, solids in the gas disk gradually migrated towards the proto-Sun on a longer timescale, ranging from thousands to million of years[29]. Therefore ^{16}O-rich dusts and ^{16}O-poor gas were mixed in different proportions. If X-ray-flare heating occurred with the fluctuation, O isotopic compositions of dusts were changed by the heating event. Thus ^{16}O-rich and ^{16}O-poor materials coexist in this fluctuation zone. This model is consistent with previous O isotopic observations: oxygen isotopic exchange of ^{16}O-rich CAI minerals with the ^{16}O-poor nebula gas can occur by heating when the CAIs are immersed in the gas[30]; the X-point fluctuations and the solid migrations allow mechanical mixing between ^{16}O-poor CAI and ^{16}O-poor chondrule solids[28].

This model indicates that CAI-forming and chondrule-forming events are not independent, but overlapped during the evolution of the early Solar System. We predict that chondrules having the same age as CAIs, or having the same ^{16}O-enrichment as CAIs, will be found in chondrites. □

Received 14 October 2002; accepted 28 April 2003; doi:10.1038/nature01699.

1. Wood, J. A. in *Chondrules and the Protoplanetary Disk* (eds Hewins, R. H., Jones, R. H. & Scott, E. R. D.) 55–69 (Cambridge Univ. Press, Cambridge, 1996).
2. Tatsumoto, M., Unruh, D. M. & Desborough, G. A. U-Th-Pb and Rb-Sr systematics of Allende and U-Th-Pb systematics of Orgueil. *Geochim. Cosmochim. Acta* **40,** 617–634 (1976).
3. Chen, J. H. & Tilton, G. R. Isotopic lead investigations on the Allende carbonaceous chondrite. *Geochim. Cosmochim. Acta* **40,** 635–643 (1976).
4. Amelin, Y., Krot, A. N., Hatcheon, I. D. & Ulyanov, A. A. Lead isotopic ages of chondrules and calcium-aluminum-rich inclusions. *Science* **297,** 1678–1683 (2002).
5. Russell, S. S., Srinivasan, G., Huss, G. R., Wasserburg, G. J. & MacPheron, G. J. Evidence for widespread ^{26}Al in the solar nebula and constraints for nebula time scales. *Science* **273,** 757–762 (1996).
6. Bischoff, A. & Keil, K. Al-rich objects in ordinary chondrites: Related origin of carbonaceous and ordinary chondrites and their constituents. *Geochim. Cosmochim. Acta* **48,** 693–709 (1984).
7. Srinivasan, G. & Bischoff, A. Magnesium-aluminum study of hibonites within a chondrule-like object from Sharps (H3). *Meteorit. Planet. Sci.* **32,** A148 (1998).
8. Krot, A. N. *et al.* Mineralogical, aluminum-magnesium, and oxygen-isotopic studies of the relic calcium-aluminum-rich inclusions in chondrules. *Meteorit. Planet. Sci.* **34,** A68–A69 (1999).
9. Maruyama, S., Yurimoto, H. & Sueno, S. Oxygen isotope evidence regarding the formation of spinel-bearing chondrules. *Earth Planet. Sci. Lett.* **169,** 165–171 (1999).
10. MacPherson, G. J., Wark, D. A. & Armstrong, J. T. in *Meteorites and the Early Solar System* (eds Kerridge, J. F. & Matthews, M. S.) 746–807 (Univ. Arizona Press, Tucson, 1988).
11. Noguchi, T. Texture and chemical composition of pyroxenes in chondrules in carbonaceous and unequilibrated ordinary chondrites. *Proc. NIPR Symp. Antarct. Meteorites* **2,** 169–199 (1989).
12. Jones, R. H., Saxton, J. M., Lyon, I. C. & Turner, G. Oxygen isotopes in chondrule olivine and isolated olivine grains from the CO3 chondrite, ALHA77307. *Meteorit. Planet. Sci.* **35,** 849–857 (2000).
13. Wasson, J. T., Rubin, A. E. & Yurimoto, H. CO chondrule evidence for a drift in the nebular oxygen-isotopic composition. [abstract]. *Meteorit. Planet. Sci.* **35,** A166–A167 (2000).
14. Stolper, E. Crystallization sequences of Ca-Al-rich inclusions from Allende: An experimental study. *Geochim. Cosmochim. Acta* **46,** 2159–2180 (1982).

15. Itoh, S., Kojima, H., Yurimoto, H.. *Lunar Planet. Sci.* **XXXI,** 1323 (2000) [CD-ROM].
16. Stolper, E. & Paque, J. M. Crystallization sequences of Ca-Al-rich inclusions from Allende: The effects of cooling rate and maximum temperature. *Geochim. Cosmochim. Acta* **50,** 1785–1806 (1986).
17. Yurimoto, H., Morioka, M. & Nagasawa, H. Diffusion in single-crystals of melilite: I. Oxygen. *Geochim. Cosmochim. Acta* **53,** 2387–2394 (1989).
18. Lasaga, A. C. in *Kinetics and Equilibrium in Mineral Reactions* (ed. Saxena, S. K.)) 81–114 (Springer, New York, 1983).
19. Wasson, J. T., Yurimoto, H. & Russell, S. S. ^{16}O-rich melilite in CO3.0 chondrites; possible formation of common, ^{16}O-poor melilite by aqueous alteration. *Geochim. Cosmochim. Acta* **65,** 4539–4549 (2001).
20. Kojima, T., Yada, S. & Tomeoka, K. Ca-Al-rich inclusions in three Antarctic CO3 chondrites, Yamato-81020, Yamato-82050 and Yamato-790992: Record of low-temperature alteration. *Proc. NIPR Symp. Antarct. Meteorites* **8,** 79–96 (1995).
21. Itoh, S., Kojima, H. & Yurimoto, H. Petrography and oxygen isotopic compositions in refractory inclusions from CO chondrites. *Geochim. Cosmochim. Acta* (in the press).
22. Shu, F. H., Shang, H., Glassgold, A. E. & Lee, T X-rays and fluctuating X-winds from protostars. *Science* **277,** 1475–1749 (1997).
23. Shu, F. H., Shang, H., Gounelle, M., Glassgold, A. E. & Lee, T. The origin of chondrules and refractory inclusions in chondritic meteorites. *Astrophys. J.* **548,** 1029–1050 (2001).
24. Gounelle, M. *et al.* Extinct radioactivities and protosolar cosmic rays: Self-shielding and light elements. *Astrophys. J.* **548,** 1051–1070 (2001).
25. Yurimoto, H., Asada, Y. & Hirai, K. Oxygen isotopic composition of fine-grained CAIs and genetic relation to coarse-grained CAIs. *Meteorit. Planet. Sci.* **36,** A230 (2001).
26. Clayton, R. N. Oxygen isotopes in meteorites. *Annu. Rev. Earth Planet Sci.* **21,** 115–149 (1993).
27. Krot, A. N., McKeegan, K. D., Leshin, L. A., MacPherson, G. J. & Scott, E. R. D. Existence of an ^{16}O-rich gaseous reservoir in the solar nebula. *Science* **295,** 1051–1054 (2002).
28. Krot, A. N. *et al.* Refractory calcium-aluminum-rich inclusions and aluminum-diopside-rich chondrules in the metal-rich chondrites Hammadah al Hamra 237 and Queen Alexandra Range 94411. *Meteorit. Planet. Sci.* **36,** 1189–1216 (2001).
29. Cameron, A. G. W. The first ten million years in the solar nebula. *Meteoritics* **30,** 133–161 (1995).
30. Yurimoto, H., Ito, M. & Nagasawa, H. Oxygen isotope exchange between refractory inclusion in Allende and solar nebula gas. *Science* **282,** 1874–1877 (1998).

Supplementary Information accompanies the paper on **www.nature.com/nature**.

Acknowledgements We thank J. T. Wasson and A. E. Rubin for loaning us the thin section and for discussions. We also thank A. Meibom, A. N. Krot and T. J. Fagan for discussions and for improving the English of this Letter. This work was supported by Monbu-Kagaku-sho grants.

Competing interests statement The authors declare that they have no competing financial interests.

Correspondence and requests for materials should be addressed to H.Y. (yuri@geo.titech.ac.jp).

Generation of nonclassical photon pairs for scalable quantum communication with atomic ensembles

A. Kuzmich, W. P. Bowen, A. D. Boozer, A. Boca, C. W. Chou, L.-M. Duan & H. J. Kimble

Norman Bridge Laboratory of Physics 12-33, California Institute of Technology, Pasadena, California 91125, USA

Quantum information science attempts to exploit capabilities from the quantum realm to accomplish tasks that are otherwise impossible in the classical domain[1]. Although sufficient conditions have been formulated for the physical resources required to achieve quantum computation and communication[2], there is a growing understanding of the power of quantum measurement combined with the conditional evolution of quantum states for accomplishing diverse tasks in quantum information science[3–5]. For example, a protocol has recently been developed[6] for the realization of scalable long-distance quantum communication and the distribution of entanglement over quantum networks. Here we report the first enabling step in the realization of this protocol, namely the observation of quantum correlations for photon pairs generated in the collective emission from an atomic ensemble. The nonclassical character of the fields is demonstrated by the violation of an inequality involving their normalized correlation functions. Compared to previous investigations of non-classical correlations for photon pairs produced in atomic cascades[7] and in parametric down-conversion[8], our experiment is distinct in that the correlated photons are separated by a programmable time interval (of about 400 nanoseconds in our initial experiments).

The theoretical proposal of ref. 6 (hereafter 'DLCZ') is a probabilistic scheme based upon the entanglement of atomic ensembles via detection events of single photons in which the sources are intrinsically indistinguishable, and generates entanglement over long distances via a quantum repeater architecture[9]. The DLCZ scheme, with built-in quantum memory and entanglement purification, is well within the reach of current experiments and accomplishes the same objectives as previous more complex protocols that require as yet unattainable capabilities[9,10].

In our experiment, we demonstrate a basic primitive integral to the DLCZ scheme. Specifically, an initial 'write' pulse of (classical) light is employed to create a state of collective atomic excitation as heralded by photoelectric detection of a first photon 1. After a programmable delay δt, a subsequent 'read' pulse interrogates the atomic sample, leading to the emission of a second (delayed) photon 2. The manifestly quantum (or nonclassical) character of the correlations between the initial 'write' photon 1 and the subsequent 'read' photon 2 is verified by way of the observed violation of a Cauchy–Schwarz inequality for coincidence detection of the (1, 2) fields[7]. Explicitly, we find $[\tilde{g}^2_{1,2}(\delta t) = (5.45 \pm 0.11)] \not\leqslant [\tilde{g}_{1,1}\tilde{g}_{2,2} = (2.97 \pm 0.08)]$, where $\tilde{g}_{i,j}$ are normalized correlation functions for the fields (i, j) and $\delta t = 405$ ns is the time separation between the (1, 2) emissions. The capabilities realized in our experiment provide an important initial step towards the implementation of the full DLCZ protocol, which would enable the distribution and storage of entanglement among atomic ensembles distributed over a quantum network. Extensions of these capabilities could facilitate scalable long-distance quantum communication[6] and quantum state engineering[11]. For example, by employing spin-polarized samples in optical-dipole or magnetic traps[12], it should be possible to extend the interval δt to times of several seconds.

Our experiment arises within the context of prior work on spin squeezing[13,14], and in particular on atomic ensembles where significant progress has been made in the development of methods to exploit collective enhancement of atom–photon interactions provided by optically thick atomic samples[15–20]. Instead of homodyne or heterodyne detection of light as used in spin-squeezing experiments[18–20], the DLCZ scheme involves photon-counting techniques, which present stringent requirements for broad bandwidth detection and for the suppression of stray light from the atomic ensemble.

As illustrated in Fig. 1, an optically thick sample of three-level atoms in a lambda-configuration is exploited to produce correlated photons via the following sequence. With atoms initially prepared in state $|a\rangle$ by optical pumping, a laser pulse from the 'write' beam tuned near the $|a\rangle \rightarrow |e\rangle$ transition illuminates the sample and induces spontaneous Raman scattering to the initially empty level $|b\rangle$ via the $|e\rangle \rightarrow |b\rangle$ transition at time $t^{(1)}$. The 'write' pulse is made sufficiently weak so that the probability to scatter one Raman photon into the preferred forward-propagating mode $\psi^{(1)}(\mathbf{r}, t)$ is much less than unity for each pulse. Detection of a photon in the mode $\psi^{(1)}(\mathbf{r}, t)$ produced by the $|e\rangle \rightarrow |b\rangle$ transition results in a single excitation in the atomic level $|b\rangle$ distributed across the

Supplementary Tables

Table S1. Additional concentration data (wt%) of mesostasis in A-5 inclusion.

	near melilite			near enstatite					
beam	rastering	spot	spot	rastering	spot	spot	spot	spot	spot
MgO	1.4	13.3	7.0	9.5	6.0	10.6	12.3	10.2	12.1
Al_2O_3	36.9	18.1	41.2	27.5	38.1	43.9	45.1	25.6	46.5
SiO_2	29.5	37.5	33.3	23.0	28.7	24.6	21.5	39.9	25.0
CaO	32.4	24.2	16.7	8.5	14.9	11.7	9.1	14.9	11.8
TiO_2	n.d.	6.3	0.6	1.5	n.d.	1.9	0.9	0.7	1.0
Cr_2O_3	n.d.	n.d.	0.3	0.7	n.d.	1.0	1.6	0.3	1.2
FeO*	n.d.	n.d.	0.3	6.5	0.5	1.2	4.8	0.7	1.6
Ni*	n.d.	n.d.	n.d.	0.6	n.d.	n.d.	n.d.	n.d.	n.d.
S	n.d.	n.d.	n.d.	0.2	n.d.	n.d.	n.d.	n.d.	n.d.
Total	100.2	99.4	99.5	77.8	88.2	94.9	95.1	92.2	99.2

Analytical methods are similar to those of Table 1. Low totals are due to the porous structure. FeO*: All Fe calculated as FeO. Ni*: All Ni calculated as Ni. n.d.: not detected (<0.1 wt%).

Table S2. Oxygen isotopic distribution (‰) in melilite clast of A-5 inclusion.

No. in Fig. S1	1†	2†	3	4	5	6	7
Distance* (μm)	2.6	7	0.9	9.7	4.4	9.7	1.8
$\delta^{17}O_{SMOW}$	-7.5	2.0	-15.8	9.5	-1.6	9.8	-15.1
σ_{mean}	2.9	2.5	2.2	2.0	3.1	3.0	2.3
$\delta^{18}O_{SMOW}$	0.2	7.7	-9.7	12.9	4.7	14.9	-9.9
σ_{mean}	1.2	1.4	1.0	1.4	1.1	2.1	1.0
$\Delta^{17}O_{SMOW}$	-7.6	-2.0	-10.8	2.8	-4.0	2.1	-9.9
σ_{mean}**	2.6	2.2	1.8	1.7	2.9	2.9	1.9

$\Delta^{17}O_{SMOW} = \delta^{17}O_{SMOW} - 0.52 \times \delta^{18}O_{SMOW}$. * Distance from surface; estimated error is ±0.7 μm. ** Covariance between $\delta^{17}O$ and $\delta^{18}O$ =1.7. † Corresponding to the same number in Table 1.

Supplementary Figure Legends

Figure S1. Magnified BSE images for mineral interfaces. **a,** melilite-mesostasis interface. The melilite assemblage has corroded surfaces adjacent to the mesostasis, and contains irregular cavities partially or completely filled with glass (also see Fig. 1). The mesostasis immediately surrounding the melilite has an appreciable enrichment of Ca component (Table 1 and supplementary Table S1). These observations show that the melilite clast is a relict that partly dissolved into the mesostasis liquid. However, because the contributions of the melting are expected to be ~15%, the changes of O isotopic ratios in the mesostasis are too small to erase the ^{16}O-rich nature of the mesostasis liquid. Craters indicated by numbers show locations of SIMS analyses corresponding those in Table 1. **b,** enstatite-mesostasis interface. The enstatite is directly adjacent to the mesostasis. The enstatite grains show concave curved surfaces (also see Fig. 1) and the mesostasis surrounding enstatite is relatively enriched in Mg component (Table 1 and supplementary Table S1). These observations suggest that the pyroxene assemblage partly dissolved into the mesostasis liquid. Detection of minor Cr_2O_3 and FeO components in the mesostasis (Table 1 and supplementary Table S1) also support the dissolution of the pyroxene assemblage. A crater indicated by number is shown the location of SIMS analysis corresponding to that in Table 1. **c,** enstatite-matrix interface. The lower side of the CAI is fragmented (Fig. 1) and the enstatite and augite grains directly border on the matrix. The matrix consists of mechanical aggregates of sub-micron size fine materials (mostly ferromagnesian silicates) distinct in texture and composition from the mesostasis. All figures are in the same magnification. Abbreviations are the same as in Fig. 1.

Figure S2. BSE image of melilite clast indicating locations of SIMS analyses. Craters indicated by numbers show locations of SIMS analyses corresponding those in Supplementary Table S2.

Figure S3. Oxygen isotopic zoning of melilite-clast rim. $\Delta^{17}O_{SMOW} = \delta^{17}O_{SMOW} - 0.52 \times \delta^{18}O_{SMOW}$. The plots are fitted by a diffusion penetration curve assuming constant surface concentration. The parameters of the curve are fitted to $2(Dt)^{1/2}$ = 7 μm, O isotopic composition on surface = -15‰ and initial O isotopic composition in melilite = 3.5‰, where D and t are oxygen self diffusion coefficient and annealing time, respectively. The surface composition is consistent with those of mesostasis indicating that the diffusion model is appropriate. Based on the penetration curve, the cooling rate of the chondrule-bearing CAI is calculated to be 30-250 K/hour if we assume that the diffusion started at liquidus temperature of the mesostasis (1823 K). Error bars correspond to standard errors ($1\sigma_{mean}$).

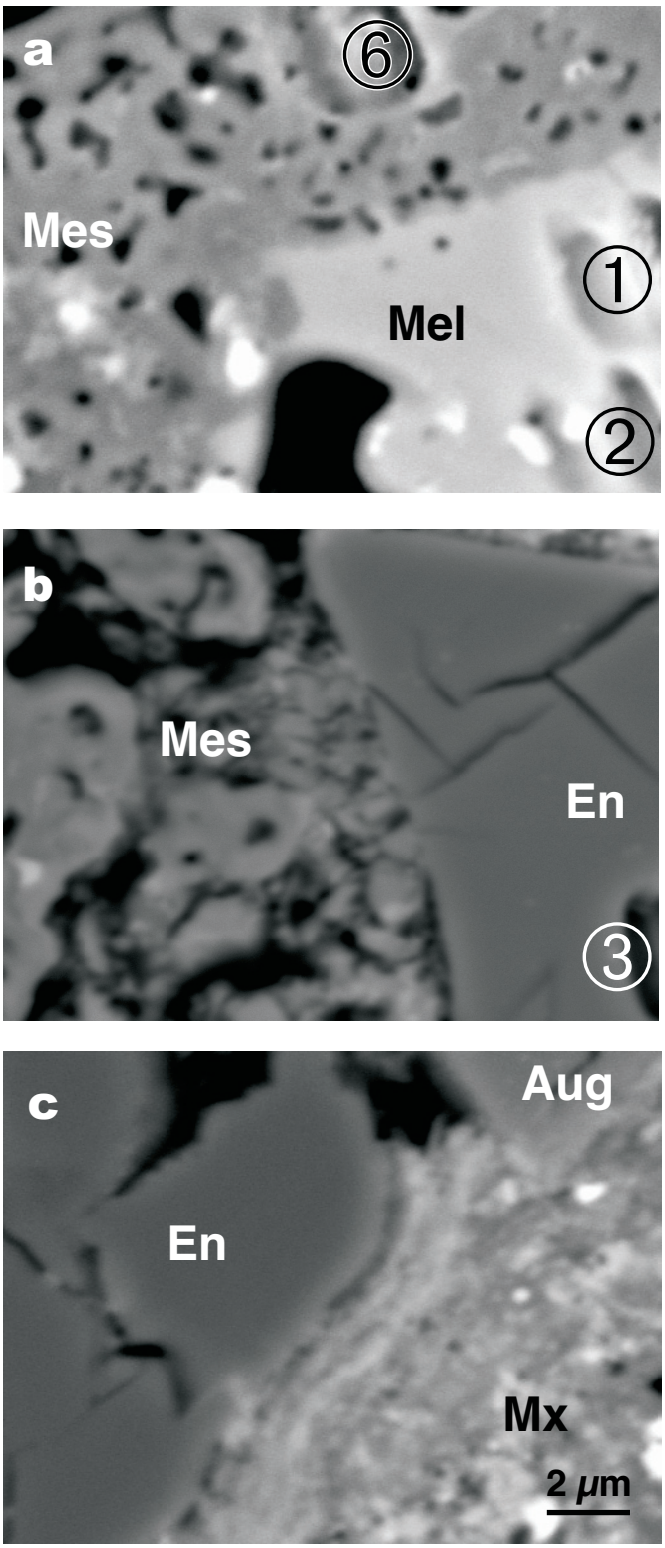
a
⑥
Mes
①
Mel
②
b
Mes
En
③
c
Aug
En
Mx
2 μm

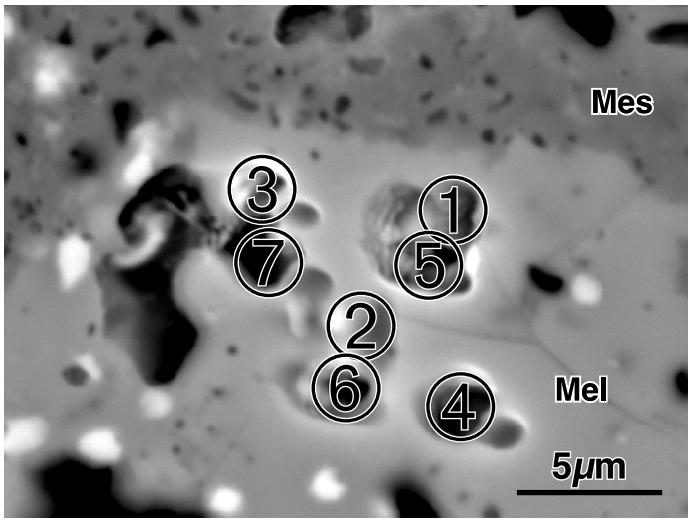
Mes
3
1
7
5
2
6
4
Mel
5μm

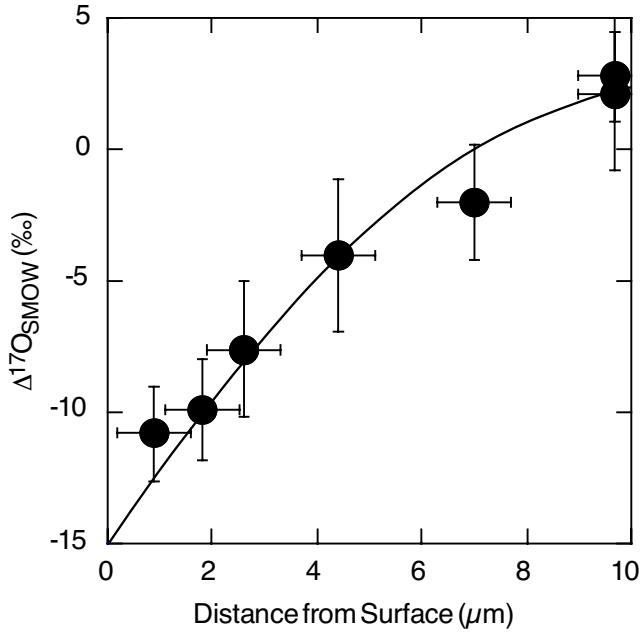
5
0
-5
-10
-15
0
2
4
6
8
10
$\Delta^{17}O_{SMOW}$ (‰)
Distance from Surface (μm)